IJMMM International Journal of Minerals, Metallurgy and Materials 矿物冶金与材料学报（英文版）

Numerical simulation of flash reduction in a drop tube reactor with variable temperatures

Yiru Yang, Qipeng Bao, Lei Guo, Zhe Wang, and Zhancheng Guo

Cite this article as:
Yiru Yang, Qipeng Bao, Lei Guo, Zhe Wang, and Zhancheng Guo, Numerical simulation of flash reduction in a drop tube reactor with variable temperatures, *Int. J. Miner. Metall. Mater.*, 29(2022), No. 2, pp. 228-238. https://doi.org/10.1007/s12613-020-2210-1

International Journal of Minerals, Metallurgy and Materials
Volume 29, Number 2, February 2022, Page 228
https://doi.org/10.1007/s12613-020-2210-1

Numerical simulation of flash reduction in a drop tube reactor with variable temperatures

Yiru Yang, Qipeng Bao, Lei Guo✉, Zhe Wang, and Zhancheng Guo✉

State Key Laboratory of Advanced Metallurgy, University of Science and Technology Beijing, Beijing 100083, China
(Received: 14 August 2020; revised: 17 October 2020; accepted: 19 October 2020)

Abstract: A computational fluid dynamics (CFD) model was developed to accurately predict the flash reduction process, which is considered an efficient alternative ironmaking process. Laboratory-scale experiments were conducted in drop tube reactors to verify the accuracy of the CFD model. The reduction degree of ore particles was selected as a critical indicator of model prediction, and the simulated and experimental results were in good agreement. The influencing factors, including the particle size (20–110 μm), peak temperature (1250–1550°C), and reductive atmosphere (H_2/CO), were also investigated. The height variation lines indicated that small particles (50 μm) had a longer residence time (3.6 s) than large particles. CO provided a longer residence time (~1.29 s) than H_2 (~1.09 s). However, both the experimental and analytical results showed that the reduction degree of particles in CO was significantly lower than that in H_2 atmosphere. The optimum experimental particle size and peak temperature for the preparation of high-quality reduced iron were found to be 50 μm and 1350°C in H_2 atmosphere, and 40 μm and 1550°C in CO atmosphere, respectively.

Keywords: flash reduction; hematite particles; drop tube reactor; numerical analysis

1. Introduction

The iron and steel industry has been identified as one of the major industrial CO_2 emitters for many years. Moreover, the huge energy consumption of the iron and steel industry has intensified emerging resource depletion issues [1−2]. However, steel cannot be completely replaced in the near future because of its high versatility and outstanding properties [3]. Many non-blast furnace ironmaking technologies have been proposed [4−8] to reduce CO_2 emissions, energy consumption, and pollution associated with the traditional ironmaking process.

The gasification–reduction coupling process is a novel alternative ironmaking technology that combines coal gasification and flash ironmaking processes. Flash ironmaking is a gas-based direct reduction process performed at high temperatures with small particles to reduce the reaction time. It has the excellent characteristics of gas-based reduction [9−10], and its high efficiency leads to a high primary reduction degree in reaction towers.

Traditional gas-based direct reduction processes (e.g., fluidized bed) are generally performed at low temperatures (500–800°C) to increase the utilization of the reducing gas [11] and avoid bonding between particles [12]. Therefore, most studies on the reduction kinetics of iron ore focused on low-temperature reduction [13−15]. In recent years, more high-temperature gas-based reduction processes have been proposed, such as the HIsarna and flash ironmaking technology [16–17]. Therefore, some researchers have investigated the high-temperature reduction process via pneumatic conveying systems. Qu *et al.* [18] studied the high-temperature reduction kinetics of fine hematite ore particles based on the HIsarna process and evaluated the unreacted shrinking core model. Sohn and Mohassab [19] utilized a high-temperature and small iron ore powder to achieve complete reduction in a very short time. Many experiments have been conducted to investigate the flash ironmaking process [20–23], and the kinetic database for hematite reduction in the range of 1150–1350°C has been established by Chen *et al.* [24–25]. Wang and Sohn [26] determined the magnitude reduction kinetic in a range of 1150–1400°C using H_2, and Elzohiery *et al.* [27] repeated the experiments in a range of 1150–1350°C. Sohn *et al.* [28] further summarize the latest kinetic expressions and parameters for the flash ironmaking process. The kinetic parameters showed significant differences before and after 1350°C. The reaction time of in-flight particles is a necessary variable in kinetic research; however, most drop tube reactors (DTRs) do not have a long constant temperature region to achieve a sufficient reaction time. Therefore, few high-temperature experiments can be conducted by different researchers to enrich the kinetic database. Given the harsh experimental conditions, the computational fluid dynamics (CFD) approach can be employed to investigate high-temperature processes. For example, Fan *et al.* [29] estab-

✉ Corresponding authors: Zhancheng Guo E-mail: zcguo@ustb.edu.cn; Lei Guo E-mail: leiguo@ustb.edu.cn

lished a CFD model based on a constant-temperature DTR to verify the hydrogen reduction rate of magnetite concentrate particles. This CFD model was applied to a laboratory flash reactor [30], and good agreement was achieved between simulation and experiments. Wang also established a gas–particle model for flash ironmaking based on the computational domain reported in the literature [31−32]. The operating conditions for flash reduction of magnetite under H_2 atmosphere were investigated to focus on the reduction behavior. Furthermore, the important water gas shift reaction was investigated in the hematite reduction process. Similar studies on blast furnace dust particles have been conducted using both experiments and mathematical modeling in which the in-flight particles were also reduced and smelted [33−34].

In this study, we conducted CFD simulations of the flash reduction process in a DTR with variable temperatures so that the in-flight particles experienced a mutative temperature process. The experiments were conducted simultaneously to verify the accuracy of our model. The peak temperature of DTRs was in the range of 1250–1550°C, which was much higher than the range in previous studies. Using the CFD model, the dropping process of particles in mutative temperature DTRs was illustrated, and different methods to obtain high-quality reduced iron were investigated.

2. Numerical model

2.1. Experimental process

Before explaining the principle of the model, we briefly introduce the experimental procedure. Fig. 1(a) shows the physical structure of the DTR used in this work. The experimental equipment consisted of three systems: particle feeding, air supply, and heating. Hematite concentrate particles were dropped from the particle inlet through a feeding device (50 mg/min). Simultaneously, pure reducing gas (CO/H_2) was injected from the side wall using a removable tube (150 mL/min). The amount of reducing gas was estimated to exceed 300% that of the complete reduction of the hematite concentrate. The drop tube comprised a 1.05 m-long corundum tube and a removable 0.3 m-long quartz tube. Four U-shaped silicon molybdenum rods were placed at the central zone for heating purposes. The particles were passed through the high-temperature zone and flash-reduced to metallic iron. Finally, the reduced particles, which were extracted after the reducing gas was evacuated by protective N_2, were collected in the removable tube.

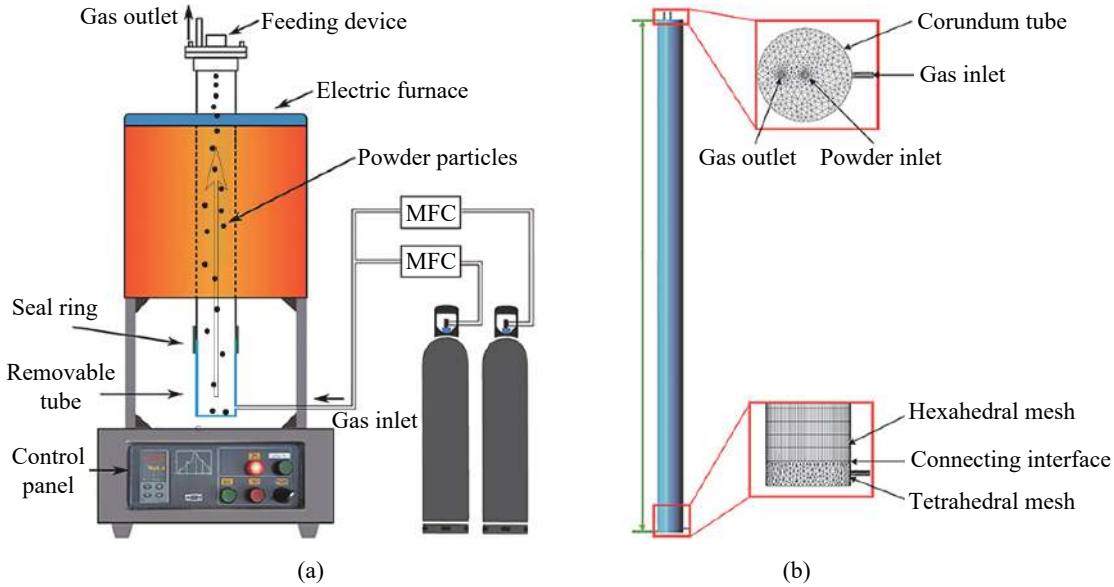

Fig. 1. Schematic of the (a) equipment structure and (b) computational domain.

A typical iron ore gas-based direct reduction process was performed, which should be recognized as countercurrent flows of reacting gas and particles from the perspective of the CFD. The Eulerian–Lagrangian method can be employed to handle this problem. The flow state of the gas was steady during the feeding time (10 min); however, the particles were tracked transiently on a time scale of 0.001 s in the computational domain.

The analytical method for the experiments included the raw material and sample characterization. The components of hematite were determined by X-ray fluorescence (XRF; ED8000, SHIMADZU, Japan), and the diameter distribution of the particles was noted using a laser particle size distribution analyzer (LMS-30; SEISHIN, Japan). The samples obtained after the reduction process were used for scanning electron microscopy and energy-dispersive X-ray spectroscopy (SEM-EDS; SUPRA 55, ZEISS, Germany). The iron content in the sample was obtained using the chemical titration method (potassium dichromate titration method, GB/T 223.7—2002); thus, the reduction degree was calculated.

2.2. Fluid flow

As previously mentioned, the feed rate of the discrete phase was 50 mg/min (9.54×10^{-3} mL/min), and the inner zone of the DTR was 4900 ml. Therefore, the volume fraction of the discrete phase was lower than 0.1% in the compu-

tational domain. The concentrate particles were treated as the dilute discrete phase. To further simplify the model, we adopted one-way coupling so that the effects of the discrete phase on the continuous phase, including the drag effect, heat transfer, and mass transfer, were neglected. By contrast, the effect of the fluid on the particles was considered.

The Reynolds number was first calculated to determine the flow state in the DTR:

$$Re = \frac{\rho u L}{\mu} \tag{1}$$

where ρ is the density (kg/m^3), u is the velocity (m/s), L is the characteristic dimension (m), that is, the diameter of the tube in this position, and μ is the viscosity (Pa·s) of the fluid. The estimated result derived from Eq. (1) indicated that the flow inside the tube was laminar. For example, the estimated Reynolds number of the cold hydrogen flow (ρ = 0.0899 kg/m^3, u = 0.00019 m/s, L = 0.065 m, and μ = 0.0101 mPa·s) in the DTR was 0.11. Therefore, the continuity and momentum equations of laminar flow were expressed as follows:

$$\frac{\partial}{\partial x_i}(\rho u_i) = 0 \tag{2}$$

$$\frac{\partial}{\partial x_j}\left(\rho u_i u_j\right) = -\frac{\partial p}{\partial x_i} + \frac{\partial}{\partial x_j}\tau_{ij} + \rho g_i \tag{3}$$

where u_i is the velocity of the fluid (m/s) in the direction i, which represents x, y in two-dimensional model and x, y, z in three-dimensional model, x_i is the distance (m), τ_{ij} is the stress tensor (Pa), and g_i is the gravity acceleration in the direction i (m/s^2).

In addition to the solution of the basic laminar flow, the temperature field should be introduced in the model to calculate the local density (ρ) in Eqs. (2) and (3). In previous CFD models, the temperature field is usually calculated separately using the heat conservation equation [29,35]. However, the radial temperature distribution in narrow DTRs can be directly ignored because of the strong radiation heat transfer. Therefore, in this work, the solution process of the temperature field was replaced by the given one-dimensional temperature distribution. The actual distributions were repeatedly measured using a K-type thermocouple at different set temperatures and modeled as a second-order polynomial function. The temperature distribution calculated using the set temperature of the DTR was coupled into the model for subsequent calculations using user-defined functions (UDFs). For simplicity, a detailed derivation process was not performed, but the predicted and measured temperature distributions were in good agreement, as shown in Fig. 2.

2.3. Particle tracking

The particle motion was tracked using the Lagrangian method, which is based on the following force balance equation:

$$\frac{\mathrm{d}u_{i,\mathrm{p}}}{\mathrm{d}t} = \frac{u_{i,\mathrm{p}} - u_i}{\tau_\mathrm{r}} + \frac{g_i(\rho_\mathrm{p} - \rho)}{\rho_\mathrm{p}} \tag{4}$$

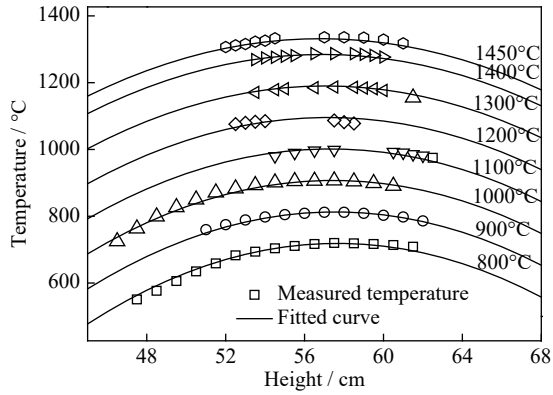

Fig. 2. Quadratic fitting results of the temperature distribution.

where $u_{i,\mathrm{p}}$ is the particle velocity (m/s), u_i is the gas velocity (m/s), ρ_p is the particle density (kg/m^3), ρ is the density of the fluid (kg/m^3), g_i is the gravitational acceleration (m/s^2), and τ_r is the relaxation time (s). The particle density depends on the composition and exerts a slight influence on the gas–solid flow. The relaxation time was calculated as follows [36]:

$$\tau_\mathrm{r} = \frac{\rho_\mathrm{p} d_\mathrm{p}^2}{18\mu}\frac{24}{C_\mathrm{D} Re} \tag{5}$$

where d_p is the particle diameter (m), μ is the molecular viscosity of the gas flow (Pa·s), Re is the particle Reynolds number in this position, and C_D is the drag coefficient described using different models [37–39]. For micron-size irregular particles, several drag models can be used to describe the drag force in the dropping process, such as the spherical model and non-spherical model. Although the shape of the ore particles was irregular, the widely applied spherical model proposed by Morsi and Alexander [37] gives the most accurate prediction of the ore particles. The expression can be written as follows:

$$C_\mathrm{D} = a_1 + \frac{a_2}{Re} + \frac{a_3}{Re^2} \tag{6}$$

where the constants a_1, a_2, and a_3 are provided over several ranges of the particle Reynolds number. In the minimal range of Re in the DTR, the expressions are as follows:

$$C_\mathrm{D} = \begin{cases} \dfrac{24}{Re}, & Re < 0.1 \\ 3.69 + \dfrac{22.73}{Re} + \dfrac{0.0903}{Re^2}, & 0.1 < Re < 1.0 \end{cases} \tag{7}$$

Besides C_D, another unknown parameter in Eq. (5) is the diameter d_p. A laser particle size analyzer was used to examine the diameter distribution of the raw ore powder. The results showed the corresponding accumulation volume fraction Y at the specific diameter d_p, indicating that the total volume fraction of particles was higher than the diameter d_p. The measured data plotted in Fig. 3 were fitted using the following Rosin–Rammler diameter distribution:

$$Y = \mathrm{e}^{-(d_\mathrm{p}/\bar{d})^n} \tag{8}$$

where $\bar{d}$ is the mean diameter (equal to 66.9 μm) obtained when the value of Y is fixed at 0.368, and n is the spread parameter. For each measured point, a specific value of the

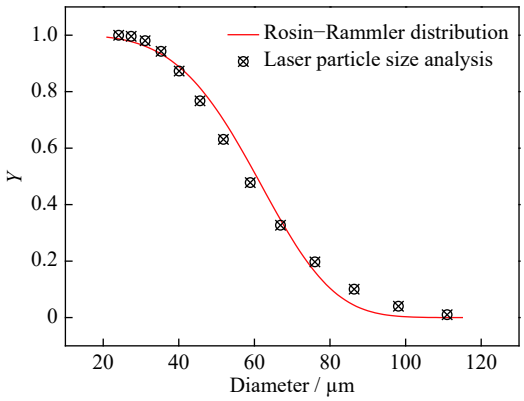

Fig. 3. Diameter distribution fitting by Rosin–Rammler expression (the red line is obtained from the distribution function, and the measured point is from the laser particle size analysis).

spread parameter n was calculated using Eq. (8), and the average value n_{avg} was adopted to fit most of the data points. Through this method, the measured particle diameter distribution was fitted using a mathematical function with a high degree of fitness. The particle size in the model was divided into eight different intervals from 20 to 110 μm to improve the accuracy of the calculations.

The heat conservation equation was further solved separately to obtain the particle temperature as follows based on the solution of particle motion:

$$m_p c_p \frac{dT_p}{dt} = hA_p(T - T_p) - \frac{dm_p}{dt}\Delta_r H_{reac} + \varepsilon_p A_p \sigma (T^4 - T_p^4) \quad (9)$$

where c_p is the specific heat of particles (J/kg·K), T_p is the particle temperature (K); h is the heat transfer coefficient (W/m^2·K); A_p is the particle surface area (m^2); $\Delta_r H_{reac}$ is the reaction heat per unit mass of the particle (J/kg); ε_p is the particle radiation emissivity, which was set to 0.8 [40]; and σ is the Stefan–Boltzmann constant. The following dimensionless correlation among the Nusselt number Nu, Reynolds number Re, and Prandtl number Pr was evaluated using the particle heat transfer coefficient h:

$$Nu = 2.0 + 0.6Re^{1/2}Pr^{1/3} = \frac{hd_p}{k_g} \quad (10)$$

where k_g denotes the thermal conductivity of the gas. The real-time particle position and temperature were tracked transiently, and all the relevant parameters for deriving the reduction reaction solution were obtained.

2.4. Reaction mechanism

The reduction kinetic mechanism is the core of the model. Various experimental conditions were used in previous studies on reduction kinetics, but the general formula of the reduction reaction was as follows [26,28,41–42]:

$$\frac{dX}{dt} = A_q e^{-E_a/RT} \cdot (d_p)^S \cdot n(1-X)[-\ln(1-X)]^{1-1/n} \cdot (P_i^m - \frac{P_j^m}{K_e}) \quad (11)$$

This general kinetic expression is composed of four terms: (1) temperature term, (2) particle size term, (3) reduction degree term, and (4) pressure term. These terms are described in the following subsections. The detailed meanings were elaborated in the following sections:

2.4.1. Temperature

The apparent Arrhenius formula ($A_q e^{-E_a/RT}$, where A_q is the pre-exponential factor, and E_a is the apparent activation energy) determines the effect of temperature on the reaction rate. In accordance with the functional characteristics, a high reaction temperature induces a fast reaction rate. The kinetic parameters can only be determined experimentally, and they are highly dependent on the experimental conditions.

2.4.2. Particle size

The influence of the particle diameter on the reduction rate can be represented as $(d_p)^s$, where d_p is the particle diameter and s is a coefficient. As the gas–solid reaction usually occurs at the interface, the reaction rate dm/dt has a positive relationship with the specific surface area S_p, which is defined as A_p/m_p. For spherical particles, the specific surface area S_p can be obtained as follows:

$$S_p = \frac{A_p}{m_p} = \frac{6\pi d_p^2}{\pi d_p^3 \rho_p} = \frac{6}{d_p \rho_p} \quad (12)$$

where A_p is the surface area (m^2), and m_p is the mass (kg) of a single particle. However, the actual mechanism is highly complex, particularly at the flash ironmaking conditions. Some researchers have pointed out that the diameter has no significant relationship with the reaction rate when the particle size is below 100 μm [29,41]. The internal diffusion was no longer a limiting factor in small particles. Therefore, the value of the coefficient s was set to 0 in this work.

2.4.3. Reduction degree

The expression $n(1-X)[-\ln(1-X)]^{1-1/n}$ defines the influence of the reduction degree X on the reduction reaction rate (nucleation model). As the reduction degree increases, the mass fraction of the ferrous oxide and the contact area decrease continuously. The value of n is usually determined by trial and error [42–43].

In this study, the constants A_q, E_a, s, and n were measured under the flash ironmaking conditions proposed by Chen *et al.* [19–20], which were compatible with our equipment. The values are listed in Table 1.

Table 1. Kinetic parameters of reduction reactions

Reaction	A_q	E_a / (kJ·mol^{-1})	s	n	m
$Fe_2O_3 + H_2 = Fe + H_2O$	4.41×10^7	214	0	1	1
$Fe_2O_3 + CO = Fe + CO_2$	1.91×10^7	231	0	1	1

2.4.4. Pressure

The influence of the partial pressure of reducing gas species i (H_2/CO) and the corresponding oxidizing product j (H_2O/CO_2) can be expressed as $P_i^m - P_j^m/K_e$, where K_e is the chemical equilibrium constant, which indicates the thermodynamic limit. The value of m depends on the stoichiometry of the reaction. However, the chemical equilibrium constant K_e is a variable for the specific reaction associated with temperature. Studies on reduction kinetic usually consider a specific value of K_e at a certain temperature T. However, the

constant K_e was not sufficiently precise in DTRs in which the temperature varied along the flow direction. The real-time equilibrium constant must be calculated with temperature changes [22].

In this study, the thermodynamic derivation process was introduced into the model to theoretically calculate the real-time equilibrium constant in the solution. The relationship between the equilibrium constant and the Gibbs free energy of a reaction was used via the thermodynamic equation. The change in the Gibbs free energy $\Delta_r G_m^{\ominus}(T)$ can be expressed as follows:

$$\Delta_r G_m^{\ominus}(T) = -RT\ln K_e \tag{13}$$

where R is the ideal gas constant, which is equal to 8.314 J/mol·K. The rightmost term of Eq. (13) was further expanded as given in Eq. (14) with the standard thermodynamic database, including $\Delta_r H_m^{\ominus}$, $\Delta_r S_m^{\ominus}$, and ΔC_p, on the basis of the definition of the Gibbs free energy:

$$\Delta_r G^{\ominus}(T) = \Delta_r H_m^{\ominus} - T\Delta_r S_m^{\ominus} + \int_{25}^{T} \Delta C_p \mathrm{d}T - \int_{25}^{T} \frac{\Delta C_p}{T}\mathrm{d}T \tag{14}$$

where $\Delta_r H_m^{\ominus}$ is the standard molar enthalpy of formation, and $\Delta_r S_m^{\ominus}$ is the standard molar generation of entropy. ΔC_p is the difference in the standard constant pressure specific heat tolerance between the reactants and the product, and it is expressed as follows:

$$\Delta C_p = \Sigma v_y C_{p,y} - \Sigma v_x C_{p,x} = \left(\Sigma v_y a_y - \Sigma v_x a_x\right) + \left(\Sigma v_y b_y - \Sigma v_x b_x\right)T \tag{15}$$

where the standard specific heat $C_{p,x}$ of species x depends on temperature, as well as $C_{p,y}$ of species y. The expressions were presented as linear fit functions based on the thermodynamic database; all the changes in the crystal form and the phase transitions were ignored.

After integrating Eq. (14), $\Delta_r G^{\ominus}(T)$ can be expressed as follows:

$$\Delta_r G^{\ominus}(T) = \Delta_r H_m^{\ominus} - T\Delta_r S_m^{\ominus} + T(\Sigma a M_0 + \Sigma b M_1) \tag{16}$$

where $M_0 = \ln(T/298.15) + 298.15/T - 1$ and $M_1 = T/2 - 298.15 - 298.15^2/(2T)$. After substituting Eq. (16) into Eq. (11), K_e can be obtained and coded into the UDFs. The corresponding equilibrium partial pressure of reducing gas obtained through the above calculations was compared with the value provided by HSC Chemistry (Fig. 4). Satisfactory agreement was obtained in the experimental temperature range. Although a certain equilibrium constant could be obtained by polynomial fitting, the analytical solution derived from the physical meaning was meaningful and adaptive.

3. Numerical details

The second-order upwind scheme was employed to discretize the governing equations, that is, the continuity and momentum equations. The classical SIMPLE algorithm was employed to handle the pressure–velocity coupling. Other scalar equations, such as species transport, were further evaluated separately. The particles were tracked simultaneously, and the interphase transfer between gas and particles was calculated. The basic solution process was completed in the commercial CFD software ANSYS Fluent. Specific submodules, including the radiation heat transfer, and chemical reaction modules were used to enhance the prediction performance. The basic information flow diagram of the CFD model is shown in Fig. 5. The important variables in the model were divided into particle (position, velocity, temperature, and species), fluid (pressure, velocity, temperature, and species), and interphase information (drag, heat transfer rate, and chemical reaction rate). These critical variables were evaluated simultaneously based on the necessary boundary conditions and updated depending on variations in other parameters. Given that the one-way coupling process was adopted, the fluid could influence the particle through interphase variables, but not vice versa. The most significant reduction degree was obtained from the particle information and experiments, and model verification was finally performed.

The pre-processing tool ICEM was used to generate a high-quality mesh. The furnace body and the intersecting structure of the top and bottom of the furnace were made of approximately 200000 hexahedral cells and 100000 tetrahedral cells, as shown in Fig. 1(b). Mesh independence was already demonstrated by comparing the axial data (x-velocity) in different cases, and detailed data were not listed for brevity.

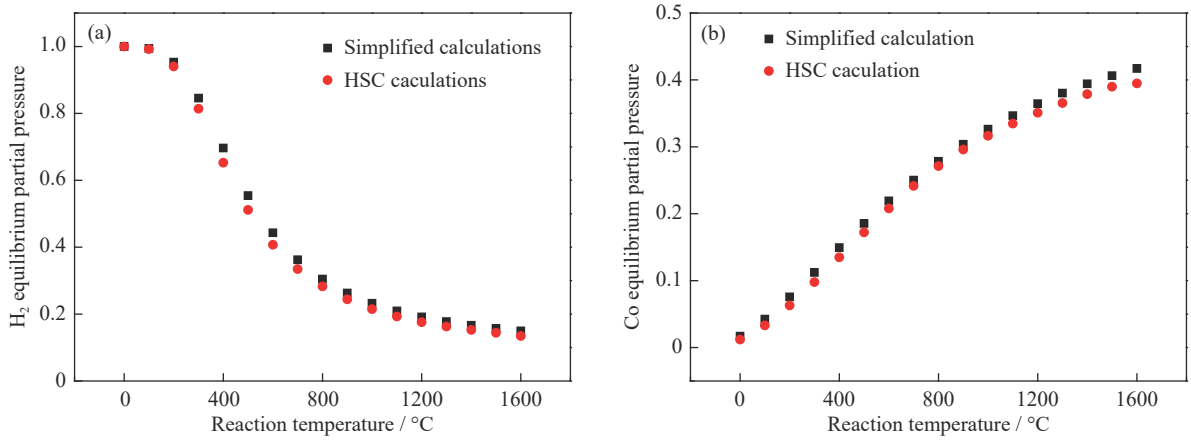

Fig. 4. Equilibrium partial pressure of reducing gases during reduction reactions obtained by simplified thermodynamic derivation calculations and HSC Chemistry calculations: (a) H_2 and (b) CO.

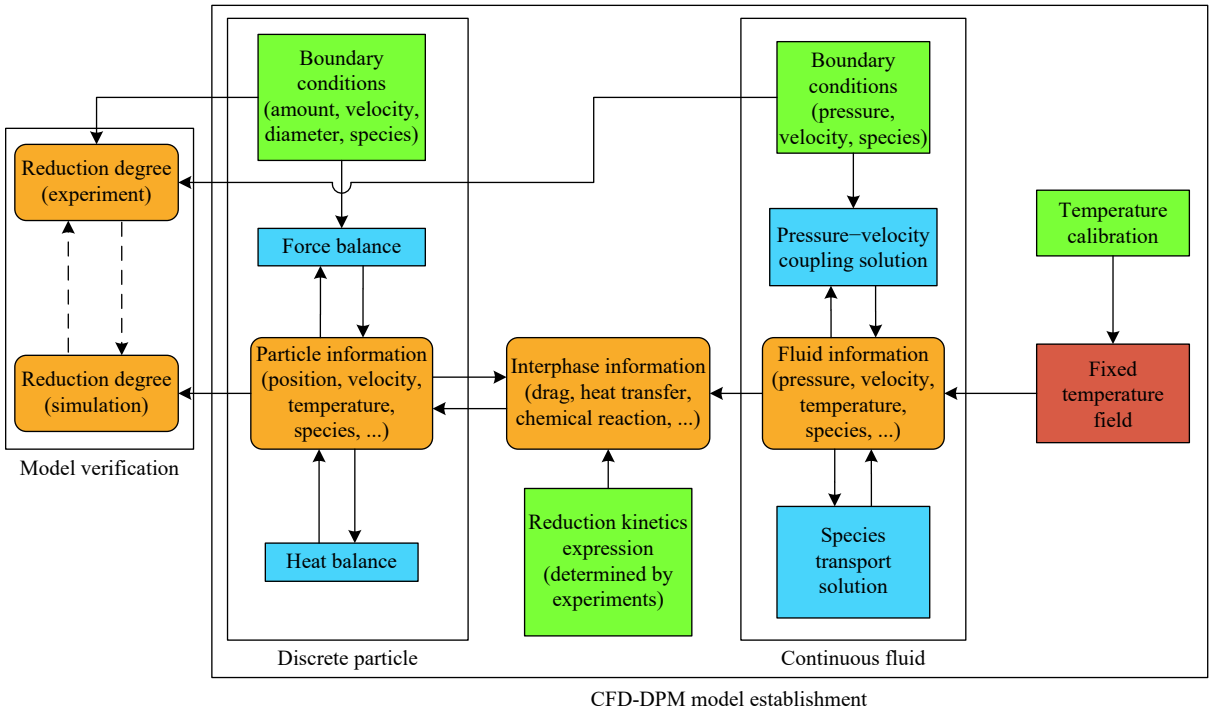

Fig. 5. Information flow diagram of the comprehensive model (green block: experimental operations, yellow block: information data, blue block: critical process, and red block: specific link to replace the temperature solution).

4. Results and discussion

4.1. Model validation

The reduction degree (X) was considered as the critical indicator to verify the accuracy of our model. It is defined as the ratio of the reduced oxygen element content to the oxygen element content in the initial iron oxide. Assuming that the gangue in the concentrate remains unchanged [44], the reduction degree can be expressed as follows:

$$X = \frac{m_i - m_t}{m_i \times w_{OiF}} \tag{17}$$

where m_i is the initial mass of concentrate particles (kg), m_t is the current mass of concentrate particles (kg), and w_{OiF} is the initial mass fraction of oxygen in iron oxide (kg). The standard chemical titration method was used to determine the metal iron element content w_{Fe} as the reduction degree is not a directly measurable value. The quantitative analysis of chemical titration was repeated three times, and no more than 2% relative error was observed. Considering the iron element conservation after the reduction, the following equation was obtained:

$$m_i w_{Fe,i} = m_t w_{Fe,t} \tag{18}$$

where $w_{Fe,i}$ is the initial mass fraction of iron in particles, $w_{Fe,t}$ is mass fraction of iron element in particles at time t, and m_t is the mass of concentrate particles at time t (kg). We substitute Eq. (18) into Eq. (17) to replace m_t. The equation of the reduction degree is expressed as follows:

$$X = \frac{m_i - m_i \times \frac{w_{Fe,i}}{w_{Fe,t}}}{m_i w_{OiF}} = \frac{w_{Fe,t} - w_{Fe_2O_3} \times \frac{M_{Fe}}{M_{Fe_2O_3}}}{w_{Fe_2O_3} \times \frac{M_O}{M_{Fe_2O_3}} \times w_{Fe,t}} \tag{19}$$

where $w_{Fe,t}$ is the mass fraction of iron element in the sample measured by chemical titration; $w_{Fe_2O_3,i}$ is the mass fraction of Fe_2O_3 (Table 2); M_z is the molecular weight, and z = Fe_2O_3, Fe, and O. The hematite concentrate particles were obtained from Companhia Vale do Rio Doce.

Table 2. Component analysis using X-ray fluorescence wt%

Fe_2O_3	SiO_2	SO_3	MnO	CaO
94.918	3.274	1.393	0.382	0.034

The mass fraction of iron element $w_{Fe,t}$ can be obtained in the numerical model by calculating the average mass fraction of a large number of particles, which is the sum of the iron element in Fe and Fe_2O_3:

$$w_{Fe,t} = w_{Fe,avg} + w_{Fe_2O_3,avg} \times \frac{M_{Fe}}{M_{Fe_2O_3}} \tag{20}$$

where the average mass fractions of metal iron $w_{Fe,avg}$ and hematite $w_{Fe_2O_3,avg}$ can be obtained directly from the simulation results. The calculated $w_{Fe,t}$ is further substituted into Eq. (19) to solve the corresponding reduction degree.

Fig. 6(a) shows the reduction degrees obtained from both experiments and numerical analysis. The reduction degree increased with temperature. The effect of H_2 reduction was observed to be consistently more significant than that of CO in the experimental temperature range (1250–1550°C). Fig. 6(b) shows a comparison of the data point and fitting function ($y = x$). The confidence of fitting was as high as 0.9027, indicating a high correlation between the simulation and experimental results. Therefore, the predicted results were accurate in the high-temperature range of 1250–1550°C.

4.2. Internal distribution

The velocity field had a significant influence on particle motion, reaction process, and predicted reduction degree. The

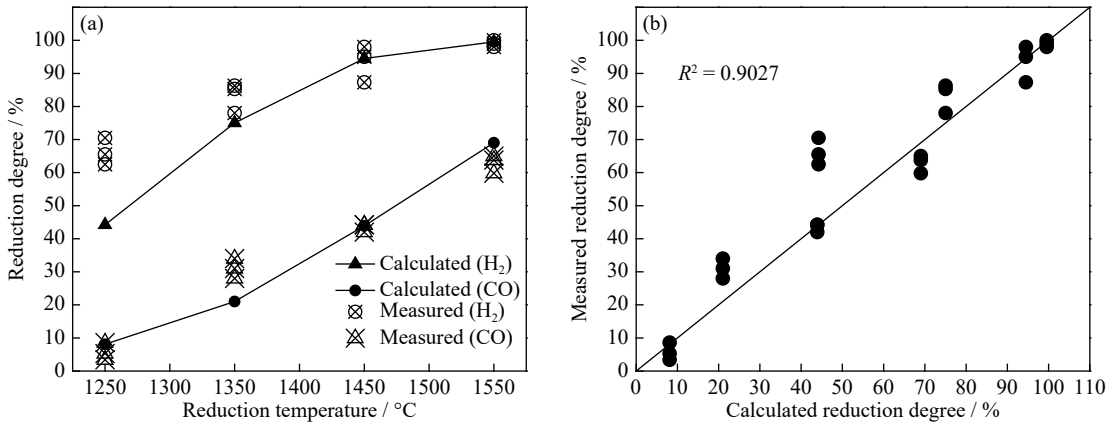

Fig. 6. Reduction degree values under different conditions: (a) experimental and simulated reduction degree values under varying temperatures and atmospheric conditions; (b) comparison of experimental and simulated reduction degree values.

velocity vector distribution on the horizontal plane conformed to typical laminar flow in a cylindrical tube, while the vertical velocity distribution was non-uniform, as shown in Fig. 7. The gas velocity in the vertical direction first increased and then decreased due to the synchronously changing temperature. According to the continuity equation Eq. (2) and the ideal gas equation, the approximately proportional relationship between the velocity and temperature can be easily inferred from the small pressure loss.

As mentioned, the vertical temperature distribution was fitted based on the measured temperature point and fixed during the reduction process. In the middle part of the drop tubes, the variation curves were similar to the temperature distribution obtained by Abolpour *et al.* [45].

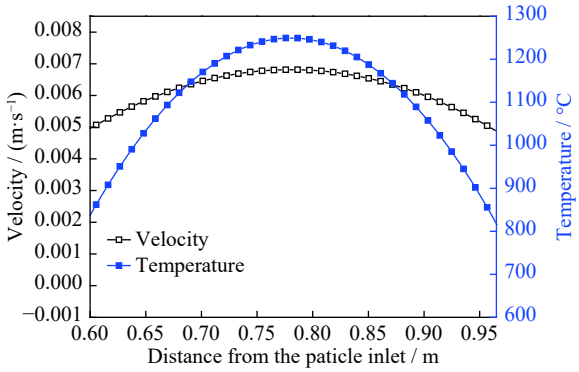

Fig. 7. Vertical velocity and temperature distribution curve on the centerline (peak temperature = 1250°C).

4.3. Particle motion

The particles can be easily tracked using the Lagrange method, and the dropping process is explained below. The dropping process of the hematite particles (100 μm) at 1250°C with pure H_2 was considered an example. Fig. 8(a) shows the particle dropping velocity (logarithmic time axis) and the height variation (both logarithmic and linear time axis). The dropping velocity increased rapidly within the first 0.1 s and was relatively stable in the subsequent dropping phase. The drag of the particles was positively correlated with the relative velocity between gas and particles. In particular, the drag of the particle increased to balance gravity, and the dropping process was converted from the acceleration stage to the force balance stage. Although significant fluctuation was noted during the force balance stage, the height–time curve in the linear coordinate could hardly be distinguished from a straight line.

Fig. 8(b) shows the dropping processes at different diameters ranging from 50 to 100 μm. As expected, particles with a smaller diameter had a longer residence time. The inset shows that the acceleration time of larger particles was significantly longer than that of smaller particles, whereas smal-

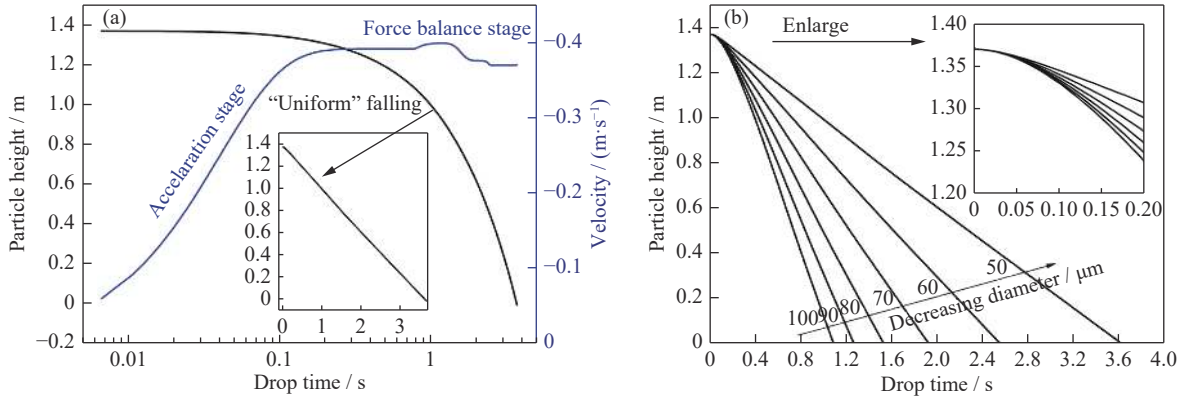

Fig. 8. Particle motion in the drop tube: (a) particle height and particle drop velocity with increasing drop time; (b) particle height variation curves at different diameters.

ler particles dropped with approximately uniform motion.

The height–time curves at different temperatures and gas compositions were also investigated, and the results are shown in Fig. 9. A specific particle size (100 μm) was considered. The comparisons indicated that the influence of temperature was not significant, and different atmospheric compositions H_2/CO led to varying residence times. For instance, the particles in CO did not touch the bottom until approximately 1.29 s, whereas the corresponding time for the particles in H_2 was only 1.02 s. These findings indicated that a high-density gaseous medium (CO) resulted in a long residence time for particles.

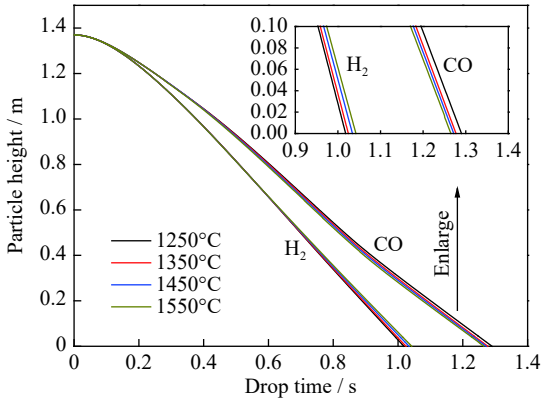

Fig. 9. Height variation curves with drop time.

4.4. Reduction process

Important parameters for the analysis of the reaction process, including the composition and temperature, can be easily obtained using the CFD method. The mass fraction of metal iron in the particles was considered an indicator of the direct metallization of the particles. The microstructure of the reduced particles varied significantly under different experimental temperatures, as shown in Fig. 10. A significant variation in structures was observed with increasing reduction degree. The fluidity of the high-temperature droplets was enhanced, and the surface tension of the liquid promoted the separation between slag and iron. The electron microscope images also showed that the FeO slag accumulated on the surface of particles.

Fig. 11(a) shows the mass fraction variation of metal iron at different heights. The ore particles were quickly reduced in a very narrow range between 0.62 and 0.95 m, which was defined as the effective reaction interval, while hardly any reaction was observed between the ore and reducing gas elsewhere. In the simulated range (50–100 μm), small particle size can continuously improve the reduction degree. Fig. 11(b) shows the reduction process of particles with different sizes over time. Even for particles with the longest residence time, the effective reaction interval was only 1.7 s. However, the hematite concentrate particles were quickly reduced in a short reaction time. Given that the reaction time of the tradi-

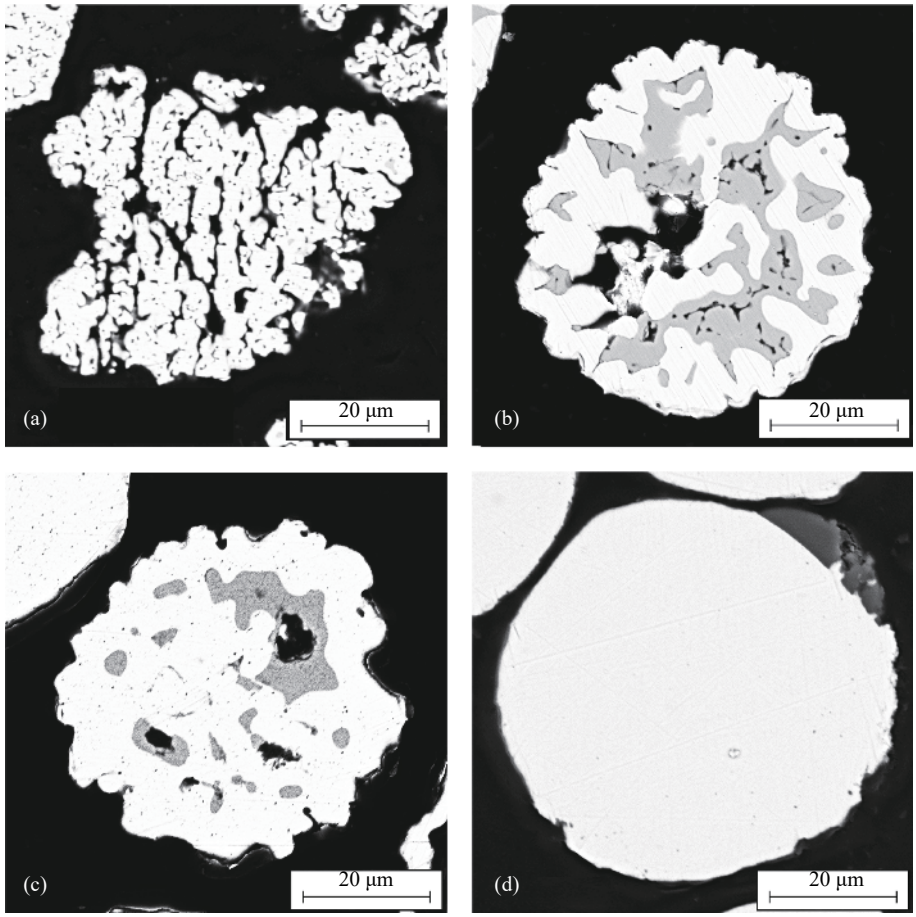

Fig. 10. SEM images of the microscopic morphologies of the products of hydrogen reduction at (a) 1250°C, (b) 1350°C, (c) 1450°C, and (d) 1550°C.

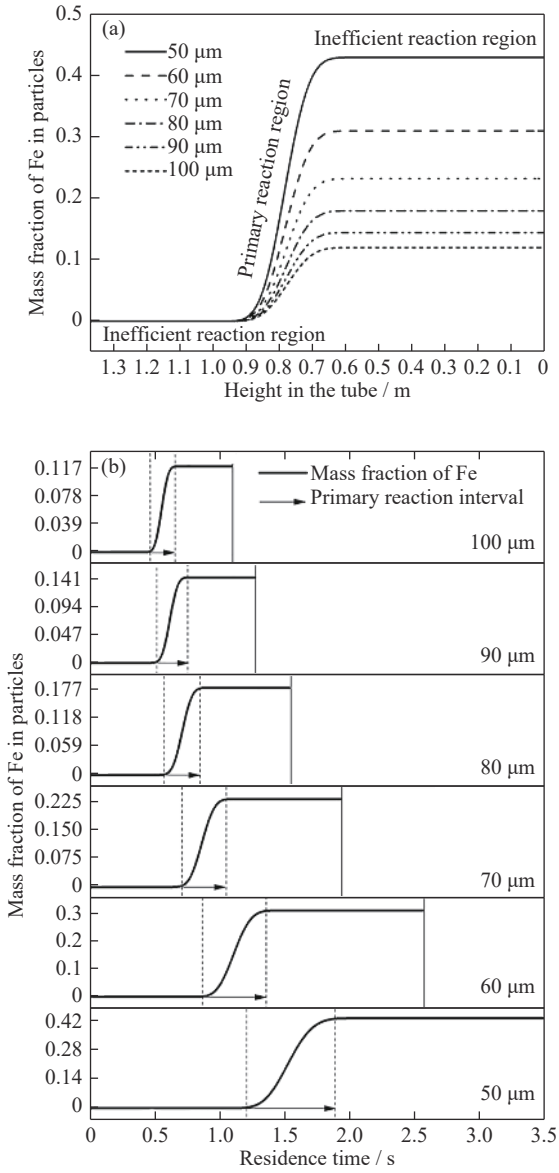

Fig. 11. Particle reduction process in DTR: (a) heights; (b) residence times.

tional direct reduction process is measured in minutes, the flash ironmaking technology is much faster than the traditional gas-based reduction.

Fig. 12 shows the reduction degree at different particle sizes, reduction temperatures, and atmospheric conditions. As the diameter increased, the reduction degree decreased continuously due to the decreasing residence times. The change in the slope indicated that the effect of diameter on the reduction degree was more significant when the particle size was small, particularly at low temperatures. A comparison of different curves revealed that a high temperature is always advantageous for the improvement in the reduction degree. Under the same temperature and particle size conditions, the reduction effect of H_2 was observed to be consistently better than that of CO, particularly at relatively low temperatures.

In summary, a temperature of at least 1350°C and a particle diameter of not larger than 50 μm are required to

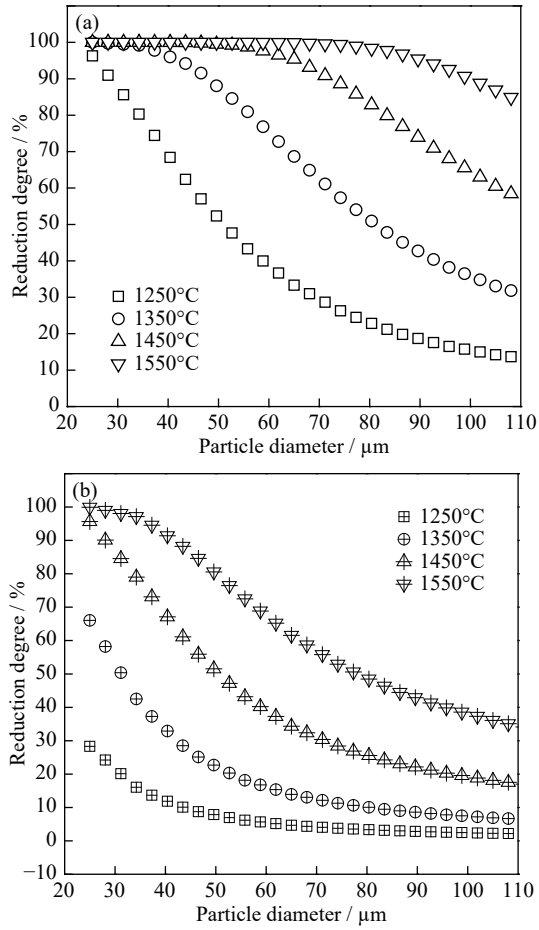

Fig. 12. Influence of particle size on the reduction degree at different temperatures and atmospheric conditions: (a) H_2 and (b) CO.

achieve a reduction degree of 90% or more in H_2 atmosphere. However, a temperature of at least 1550°C and a particle diameter of not more than 40 μm are required for the same reduction degree in CO atmosphere. These two schemes were considered the lowest requirements to obtain high-quality flash-reduced iron by using our laboratory-scale DTR at the current feeding rate.

5. Conclusions

We established a three-dimensional steady-state numerical model to simulate gas–particle countercurrent flow, heat transfer, and specific chemical reactions for the flash reduction process of hematite concentrate particles. A comparison of simulated and experimental results demonstrated the accuracy of our model. Further numerical research on a pilot-scale gasification–reduction coupling process will be conducted based on the flash reduction model proposed in this study. The other simulation results are as follows.

The gas flow in the tube was determined to be laminar based on the Reynolds number. In the axial direction, it first increased and then decreased, and it was positively correlated with variation in the temperature distribution. The CFD model revealed the dropping process of the particles. The results indicated that small particles had a long residence time,

as demonstrated by the height variation lines. The temperature and species of the gas phase also had a slight influence on the particle dropping process.

The proposed model showed that a high reduction degree could be obtained by employing a high reduction temperature, small particle size, and hydrogen atmosphere. To achieve a reduction degree of 90% or more, a temperature of at least 1350°C and a particle diameter of not more than 50 μm are required in H_2 atmosphere. By contrast, a temperature of at least 1550°C and a particle diameter of not more than 40 μm are required in CO atmosphere due to the difficulty in screening and the possible bonding effects of small particles.

Acknowledgements

This work was financially supported by the National Key Research and Development Project (No. 2016YFB0601304) and the National Natural Science Foundation of China (No. 51804030).

Conflict of Interest

The corresponding author states that there is no conflict of interest.

References

[1] C.B. Xue and D.Q. Cang, A brief overview of low CO_2 emission technologies for iron and steel making, *J. Iron Steel Res. Int.*, 17(2010), No. 3, p. 1.

[2] M.A. Quader, S. Ahmed, R.A.R. Ghazilla, S. Ahmed, and M. Dahari, A comprehensive review on energy efficient CO_2 breakthrough technologies for sustainable green iron and steel manufacturing, *Renewable Sustainable Energy Rev.*, 50(2015), p. 594.

[3] M. Naito, K. Takeda, and Y. Matsui, Ironmaking technology for the last 100 years: deployment to advanced technologies from introduction of technological know-how, and evolution to next-generation process, *ISIJ Int.*, 55(2015), No. 1, p. 7.

[4] A. Hasanbeigi, M. Arens, and L. Price, Alternative emerging ironmaking technologies for energy-efficiency and carbon dioxide emissions reduction: a technical review, *Renewable Sustainable Energy Rev*, 33(2014), p. 645.

[5] K. Meijer, C. Zeilstra, C. Teerhuis, M. Ouwehand, and J. van der Stel, Developments in alternative ironmaking, *Trans. Indian Inst. Met.*, 66(2013), No. 5, p. 475.

[6] J. Tang, M.S. Chu, F. Li, C. Feng, Z.G. Liu, and Y.S. Zhou, Development and progress on hydrogen metallurgy, *Int. J. Miner. Metall. Mater.*, 27(2020), No. 6, p. 713.

[7] Y.J. Wang, H.B. Zuo, and J. Zhao, Recent progress and development of ironmaking in China as of 2019: An overview, *Ironmaking Steelmaking*, 47(2020), No. 6, p. 640.

[8] X.L. Xi, M. Feng, L.W. Zhang, and Z. R. Nie, Applications of molten salt and progress of molten salt electrolysis in secondary metal resource recovery, *Int. J. Miner. Metall. Mater.*, 27(2020), No. 12, p. 1599.

[9] F. Li, Q.J. Zhao, M.S. Chu, J. Tang, Z.G. Liu, J.X. Wang, and S.K. Li, Preparing high-purity iron by direct reduction–smelting separation of ultra-high-grade iron concentrate, *Int. J. Miner. Metall. Mater.*, 27(2020), No. 4, p. 454.

[10] C. Feng, M.S. Chu, J. Tang, and Z.G. Liu, Effects of smelting parameters on the slag/metal separation behaviors of hongge vanadium-bearing titanomagnetite metallized pellets obtained from the gas-based direct reduction process, *Int. J. Miner. Metall. Mater.*, 25(2018), No. 6, p. 609.

[11] T. Zhang, C. Lei, and Q.S. Zhu, Reduction of fine iron ore via a two-step fluidized bed direct reduction process, *Powder Technol.*, 254(2014), p. 1.

[12] L. Guo, Y.W. Zhong, J.T. Gao, Z.R. Yang, and Z.C. Guo, Influence of coating MgO with coprecipitation method on sticking during fluidized bed reduction of Fe_2O_3 particles, *Powder Technol.*, 284(2015), p. 210.

[13] A. Pineau, N. Kanari, and I. Gaballah, Kinetics of reduction of iron oxides by H_2: Part I: Low temperature reduction of hematite, *Thermochim. Acta*, 447(2006), No. 1, p. 89.

[14] A. Pineau, N. Kanari, and I. Gaballah, Kinetics of reduction of iron oxides by H_2: Part II. Low temperature reduction of magnetite, *Thermochim. Acta*, 456(2007), No. 2, p. 75.

[15] W.K. Jozwiak, E. Kaczmarek, T.P. Maniecki, W. Ignaczak, and W. Maniukiewicz, Reduction behavior of iron oxides in hydrogen and carbon monoxide atmospheres, *Appl. Catal. A*, 326(2007), No. 1, p. 17.

[16] L. Guo, J.T. Gao, S.P. Zhong, Q.P. Bao, Z.C. Guo. *In situ* observation of iron ore particle reduction above 1373 K by confocal microscopy, *J. Iron Steel Res. Int.*, 26(2018), No. 1, p. 32.

[17] L.Y. Xing, Y.X. Qu, C.S. Wang, L. Shao, and Z.S. Zou, Gas–liquid reduction behavior of hematite ore fines in a flash reduction process, *Metall. Mater. Trans. B*, 51(2020), No. 3, p. 1233.

[18] Y.X. Qu, Y. X.Yang, Z.S. Zou, C. Zeilstra, K. Meijer, and R. Boom, Reduction kinetics of fine hematite ore particles with a high temperature drop tube furnace, *ISIJ Int.*, 55(2015), No. 5, p. 952.

[19] H.Y. Sohn and Y. Mohassab, Development of a novel flash ironmaking technology with greatly reduced energy consumption and CO_2 emissions, *J. Sustainable Metall.*, 2(2016), No. 3, p. 216.

[20] H.Y. Sohn and S.E. Perez-Fontes, Computational fluid dynamics modeling of hydrogen−oxygen flame, *Int. J. Hydrogen Energy*, 41(2016), No. 4, p. 3284.

[21] Q. Wang, G.Q. Li, W. Zhang, and Y.X. Yang, An investigation of carburization behavior of molten iron for the flash ironmaking process, *Metall. Mater. Trans. B*, 50(2019), p. 2006.

[22] M.Y. Mohassab-Ahmed and H.Y. Sohn, Application of spectroscopic analysis techniques to the determination of slag structures and properties: Effect of water vapor on slag chemistry relevant to a novel flash ironmaking technology, *JOM*, 65(2013), No. 11, p. 1559.

[23] M.Y. Mohassab-Ahmed and H.Y. Sohn, Effect of water vapor content in H_2−H_2O−CO−CO_2 mixtures on the activity of iron oxide in slags relevant to a novel flash ironmaking technology, *Ironmaking Steelmaking*, 41(2013), No. 9, p. 575.

[24] F. Chen, Y. Mohassab, T. Jiang, and H.Y. Sohn, Hydrogen reduction kinetics of hematite concentrate particles relevant to a novel flash ironmaking process, *Metall. Mater. Trans. B*, 46(2015), No. 3, p. 1133.

[25] F. Chen, Y. Mohassab, S.Q. Zhang, and H.Y. Sohn, Kinetics of the reduction of hematite concentrate particles by carbon monoxide relevant to a novel flash ironmaking process, *Metall. Mater. Trans. B*, 46(2015), No. 4, p. 1716.

[26] H.T. Wang and H.Y. Sohn, Hydrogen reduction kinetics of magnetite concentrate particles relevant to a novel flash ironmaking process, *Metall. Mater. Trans. B*, 44(2013), No. 1, p. 133.

[27] M. Elzohiery, H.Y. Sohn, and Y. Mohassab, Kinetics of hydrogen reduction of magnetite concentrate particles in solid state relevant to flash ironmaking, *Steel Res. Int.*, 88(2017), No. 2, p. 1600133.

[28] H.Y. Sohn, Energy Consumption and CO_2 emissions in ironmaking and development of a novel flash technology, *Metals*,

10(2019), No. 1, p. 54.
[29] D.Q. Fan, Y. Mohassab, M. Elzohiery, and H.Y. Sohn, Analysis of the hydrogen reduction rate of magnetite concentrate particles in a drop tube reactor through CFD modeling, *Metall. Mater. Trans. B*, 47(2016), No. 3, p. 1669.
[30] D.Q. Fan, H.Y. Sohn, Y. Mohassab, and M. Elzohiery, Computational fluid dynamics simulation of the hydrogen reduction of magnetite concentrate in a laboratory flash reactor, *Metall. Mater. Trans. B*, 47(2016), No. 6, p. 3489.
[31] X.N. Wang, G.Q. Fu, W. Li, and M.Y. Zhu, Numerical simulation of effect of operating conditions on flash reduction behaviour of magnetite under H_2 atmosphere, *Int. J. Hydrogen Energ*, 44(2019), No. 48, p. 26261.
[32] X.N. Wang, G.Q. Fu, W. Li, and M.Y. Zhu, Numerical analysis of effect of water gas shift reaction on flash reduction behavior of hematite with syngas, *ISIJ Int.*, 59(2019), No. 12, p. 2193.
[33] J. Xu, N. Wang, Z.Y. Zhou, M. Chen, and P.F. Wang, Experimental and numerical studies of the gas-molten reduction behavior of blast furnace dust particles during in-flight process, *Powder Technol.*, 361(2020), p. 226.
[34] J. Xu, N. Wang, M. Chen, Z.Y. Zhou, and P.F Wang, Evaluation of reduction behavior of blast furnace dust particles during in-flight process with experiment aided mathematical modeling, *Appl. Math. Modell.*, 75(2019), p. 535.
[35] M. Simone, E. Biagini, C. Galletti, and L. Tognotti, Evaluation of global biomass devolatilization kinetics in a drop tube reactor with CFD aided experiments, *Fuel*, 88(2009), No. 10, p. 1818.
[36] A.D. Gosman and E. Loannides, Aspects of computer simulation of liquid-fueled combustors, *J. Energy*, 7(1983), No. 6, p. 482.
[37] S.A. Morsi and A.J. Alexander, An investigation of particle trajectories in two-phase flow systems, *J. Fluid Mech.*, 55(1972), No. 2, p. 193.
[38] A. Haider and O. Levenspiel, Drag coefficient and terminal velocity of spherical and nonspherical particles, *Powder Technol.*, 58(1989), No. 1, p. 63.
[39] H. Ounis, G. Ahmadi, and J.B. McLaughlin, Brownian diffusion of submicrometer particles in the viscous sublayer, *J. Colloid Interface Sci.*, 143(1991), No. 1, p. 266.
[40] Y.B. Hahn and H.Y. Sohn, Mathematical modeling of sulfide flash smelting process: Part I. Model development and verification with laboratory and pilot plant measurements for chalcopyrite concentrate smelting, *Metall. Mater. Trans. B*, 21(1990), No. 6, p. 945.
[41] H.S. Chen, Z. Zheng, and W.Y. Shi, Investigation on the kinetics of iron ore fines reduction by CO in a micro-fluidized bed, *Procedia Eng.*, 102(2015), p. 1726.
[42] H.S. Chen, Z. Zheng, Z.W. Chen, W.Z. Yu, and J.R. Yue, Multistep reduction kinetics of fine iron ore with carbon monoxide in a micro fluidized bed reaction analyzer, *Metall. Mater. Trans. B*, 48(2017), No. 2, p. 841.
[43] D.B. Guo, Y.B. Li, B.H. Cui, Z.H. Chen, S.P. Luo, B. Xiao, H.P. Zhu, and M. Hu, Direct reduction of iron ore/biomass composite pellets using simulated biomass-derived syngas: experimental analysis and kinetic modelling, *Chem. Eng. J.*, 327(2017), p. 822.
[44] E.A. Mousa and S. Ghali, Factorial design analysis of reduction of simulated iron ore sinter reduced with CO gas at 1000–1100°C, *Ironmaking Steelmaking*, 42(2014), No. 4, p. 311.
[45] B. Abolpour, M.M. Afsahi, A. Soltani Goharrizi, and M. Azizkarimi, Simulating reduction of in-flight particles of magnetite concentrate by carbon monoxide, *Ironmaking Steelmaking*, 44(2017), No. 10, p. 750.